The

FIES Camera

equipped with E2V CCD42-40-1-B83, ser. no. 01064-17-04
Pre-commissioning characterisation

Anton Norup Sørensen
Copenhagen University Observatory

October 2003

Contents

1 Introduction

This report presents the pre-commissioning characterisation results of the CCD camera for FIES. The CCD is a E2V CCD42-40-1-B83, ser. no. 01064-17-06. It is back-side illuminated with 2048^2 imaging pixels, each $13.5\mu m$ square. The detector has two outputs, which can be used simultaneously. The camera is cooled by a Cryotiger system, also described below.

2 Cosmetics

Flat fields for wavelengths of 1060nm, 550nm and 334nm are shown in figures 1, 2 and 3, respectively.

In the central optical band, around 550nm, uniformity is very good, with a typical structure amplitude of ±0.5%. A stitching pattern is visible as three horisontal lines, but this flat fields out fine. Spots with low sensitivity are very few. In these test exposures, a bright spot appears in the middle of the field. This is purely scattered light in the setup, and not a feature of the detector. Some shadows from dust specks on the test dewar window can be seen.

At the longest wavelengths, uniformity is poorer, with variations at the +10 / -3% level. The variatios seem to be related to reflecting layers below the sensitive layer, perhaps unevenly distributed bonding material. At the bottom, fans of light are reflected off the bonding wires.

At 334nm, a highly regular pattern appears, already faintly seen at 550nm, probably from a laser annealing process. The amplitude of the pattern is about ±5%, and on top is a large scale pattern of similar amplitude. This leaves the short wavelength response rather uneven.

A similar measure of flat field quality is the Pixel Response Non-Uniformity (PRNU). This was determined for a 400 by 400 pixel segment along with QE measurements, and is displayed as vertical bars in figure 10. Worst PRNU of 3.1% is found in the near-UV at 334nm and 366nm. It then improves in the visual and near-IR band, where PRNU is almost constant at 1.0%. The values are in agreement with the E2V test sheet results and well within specifications.

Charge traps and bad columns can be found by comparing a flat field exposure at very low illumination level to a well exposed one, as illustrated in figure 4. Several exposures at $20e^-$ and $25Ke^-$ were combined to produce two high S/N flat field maps for the comparison.

It was not possible to identify any traps at all in this way, either in the imaging area or in the interface to the serial register. A conservative estimate of the detection threshold is the same as the low-level flat field illumination of $20e^-$. Some spikes can be seen in the horizontal profile of a dark exposure, shown in figure 17. This suggests that a few very low level traps do exist.

3 Read-out noise

The detector voltages were modified to optimise read-out noise (RON) without compromising linearity, and gain was adjusted to avoid influence from quantisation noise in high-gain mode. The following table shows the resulting RON found in different amplifier configurations.

	Amplifier A	Amplifier B
High gain:	$3.00 \pm 0.05e^-$	$3.38 \pm 0.05e^-$
Low gain:	$3.28 \pm 0.05e^-$	$3.55 \pm 0.05e^-$

The test sheet from E2V gives 3.6 e^- in A and 3.7 e^- in B, apparently without optimisation. A faint interference pattern can be seen in amplifier B, probably explaining why the RON is slightly worse here. Low-gain RON is higher due to a stronger impact from quantisation noise.

4 Cross-talk

In dual read-out mode, cross-talk can occur between the two output circuits. An image of a star in one side of the image will then have a faint electronic ghost image mirrored around the border of the two image sections.

A pin-hole was imaged in one channel, at an illumination level of approx. 15Ke$^-$/pixel. The image was then sought for in the opposite channel, with ten exposures summed in order to detect faint features.

For both channels, no ghost image was detected.

5 Gain, linearity and full-well

Gain, the conversion factor from Analog to Digital Units (ADU) and electrons was determined by analysis of photon noise statistics. The following conversion factors were found:

	Amplifier A	Amplifier B
High gain:	$0.74 \pm 0.01 e^-$/ADU	$0.81 \pm 0.01 e^-$/ADU
Low gain:	$1.35 \pm 0.02 e^-$/ADU	$1.35 \pm 0.02 e^-$/ADU

The data for gain determination are shown in the upper part of figures 5, 6, 7 and 8. Here the gain is determined from the average level measured over a wide illumination range.

Gain determination from noise analysis has proven to be too inaccurate for linearity measurements. In stead, linearity deviations are examined by measuring the ADU level versus exposure time, using a stable light source. Measurements made in this way are plotted in the lower half of the linearity figures. By dividing the counts with the exposure time, corrected for shutter delay, a linear response should result in a constant level.

- Amplifier A, high gain is linear to within ± 0.5% from 130e$^-$ to 47Ke$^-$ (180 – 64KADU). Linearity seems to improve towards high counts. At the lowest count levels measured, the deviation increases to about 2% at 40e$^-$.

- Amplifier B, high gain is linear to within ± 0.5% from 100e$^-$ to 52Ke$^-$ (120 – 64KADU). While still with good linearity at the highest levels, a 0.5% deviation set in above 20Ke$^-$. At the lowest count levels measured, the deviation increases to about 1.4% at 40e$^-$.

- Amplifier A, low gain is linear to within ± 0.5% from 190e$^-$ to 85Ke$^-$ (140 – 62KADU). Just before the digital saturation sets in, linearity degrades rapidly. Count levels above 60KADU should be avoided. At low levels, linearity deviation inrcreases, and is 4% at 40e$^-$.

- Amplifier B, low gain is linear to within ± 0.25% from 40e$^-$ to 51Ke$^-$ (160 – 38KADU). Above 38KADU, non-linearity increases steadily, and reaches 2.5% at 73Ke$^-$. Unlike the measurements in other configurations, this setup keeps good linearity down to the lowest level, but departs relatively early at high levels.

Generally, the linearity deviations at the lowest count levels mentioned here are likely to be partly caused by imperfect bias level subtraction.

The full well in high gain mode is defined by the digital saturation at 2^{16}ADU, about 65KADU. In low gain, a strong deviation from linearity occurs above 80Ke$^-$ for amplifier A and 60Ke$^-$ for amplifier B, due to output amplifier behaviour. The pixel charge handling capacity is significantly higher. A precise measurement was not possible, but charge blooming appears to start at a level of 200Ke$^-$ per pixel.

6 Charge Transfer Efficiency

The fraction of electrons that are successfully moved from one pixel to another during read-out is described by the charge transfer efficiency (CTE).

The CTE has been measured using a ^{55}Fe X-ray source, whose emissions generate a specific number of photo-electrons on the CCD for each detection. The read-out counts as a function of position on the CCD can then be converted to a CTE value.

The values found at detector temperatures of $-120°C$ and $-100°C$ are:

$-120°C$:	Amplifier A	Amplifier B
Serial CTE:	0.999991	0.999990
Parallel CTE:	0.999999	0.999999

$-100°C$:	Amplifier A	Amplifier B
Serial CTE:	0.999988	0.999986
Parallel CTE:	1.000000	1.000000

The uncertainty on the measurements is 10^{-6}, which means that the measured CTE is the same through both amplifiers.

The E2V test sheet quote a serial CTE of 0.999991 in amplifier A and B, and a parallel CTE of 0.999999, all measured at $-100°C$. Our measurements at $-120°C$ agree very well with this, but as the serial CTE is only marginally within specifications of a minimum of 0.99999, we tried a mesurement also at $-100°C$. At the higher temperature, one would generally expect improved CTE, as the traps hold on to the charge for a shorter time. We do see a small improvement in the already good parallel CTE, but the serial CTE only degrades further.

7 Quantum-efficiency

The sensitivity has been measured through 11 narrow-band filters from 334nm to 1060nm and is plotted as a solid line in figure 10. The horisontal bars on the measurement points is the FWHM of the filters used.

Also shown are the E2V 42-40 minimum specifications and the E2V test data, both for a detector temperature of $-30°C$. As we operate at $-120°C$, the near-IR QE drops below the warm data. Also around 650nm, we measure a QE that is marginally below specifications. In contrast, we find a higher sensitivity at blue and near-UV wavelengths, compared to the E2V measurements. It is unclear whether this is a real temperature dependency of the detector.

Pixel Response Non-Uniformity (PRNU) was determined from the same exposures. This is shown as vertical bars in the QE graph. Note that the PRNU amplitude shown is not scaled by the QE.

Stability of the sensitivity:

QE was measured twice, 5 days apart, where the detector has been heated to room temperature and the cryostat has been opened in between. As shown in figure 10, the sensitivity appears unchanged during this period.

A degrading QE is unlikely to appear at a uniform rate over the detector. The most efficient method for checking QE stability is therefore to examine the differences in flat fields obtained some time apart. The change in local structure can be examined in figure 1 for 1060nm light, figure 2 for 550nm and figure 3 for 334nm. These flat fields were made simultaneously with the QE measurements, i.e. 5 days apart.

The features immediately visible in the ratio images are dark specks from new grains of dust on the camea window, and a slight shift of the patch of scattered light in the middle. Apart from this, the 1060 and 550nm flats appear completely unchanged. At 334nm, the chequred

pattern is faintly visible in the ratio image, at sub-percent level. The uniform distribution and low level of this pattern does not make it a certain sign of QE instability, though.

Temperature dependency

The temperature of the detector can affect the quantum efficiency. There are many subtle dependencies, but the most important factor is that the bandgap to the valence level increases as the temperature drops. This means a degrading QE for the low energy near-infrared radiation. The temperature dependence of the QE has been examined by making QE measurements at -120°C and -100°C. The difference in absolute QE is slight, as can be seen in figure 10, but the relative gain is quite dramatic, as plotted in figure 11. The flat field structure depends somewhat on the temperature. While no changes are seen at 550nm, the overall QE increase at 334nm creates a change of the strength of the chequred pattern of about 1%, as can be seen in figure 13. At 1060nm, as shown in figure 12, there is a sub-percent change at the border between the high and low QE regions, and the refections off the bonding wires do not go quite as deep at -100°C.

Increased dark current may be a problem at the higher temperature, though.

8 Fringes

At long wavelengths where the detector is partially transparent, internal reflections will cause interference, making QE change rapidly with wavelength and make the local variations strong for monochromatic light. An example flat field is shown in figure 14, where the E2V CCD is illuminated by 830nm monochromatic light.

A detailed characterisation was not made for this device, but in stead data from two other CCD42-40s are presented. To characterize the fringing behavior, flat fields were made using 670nm and 830nm lasers, and monochromator illumination spanning the range 620nm to 1050nm in steps of about 50nm and with a bandwidth of approx. 2nm. Fringe amplitude was determined the standard deviation of band-pass processed flat fields. The results are plotted in figure 15. It is evident that the monochromator fringe amplitude is much smaller than the laser fringe amplitude, due to the difference in bandwidth. The laser fringes are believed to be the best representation of narrow-band sources in the sky, and the monochromator curve can be used to mark the general dependence on wavelength.

If fringing is a severe problem, increasing the detector temperature may help some. The higher opacity (QE) at warmer temperatures will cause weaker fringes.

9 Modulation Transfer Function

Data for measurement of the Modulation Transfer Function have been measured for another CCD42-40 from the same production batch. Assuming that the MTF characteristics are similar, these results are presented here. The MTF is measured registering the contrast of fringes of different spatial wavelengths projected onto the CCD.

The measured MTF is shown in figure 16 for illumination wavelengths of 670nm and 830nm. In the same figure, the expected MTF due to the pixel geometry is shown. The CCD42-40 performs well and in much of the spatial frequency range very close to the theoretical limit. Another sign of good performance is the absense of a significant colour dependence.

10 Bias and overscan

The CCD has hardware overscan regions of 50 columns at each end of the serial register. These regions should be sufficient for accurate tracking of the bias level during single and dual amplifier readout.

In addition, "extended" overscan can be used, but only for read-out windows extending to the edge of the CCD opposite of the amplifier being used, as it is generated by continued clocking and read-out after the last image column. Post-processing by BIAS will always make the extended overscan appear at the right border of the image, whatever amplifier is specified.

The bias structure in vertical direction can develop considerable gradients. During a sequence of bias exposures, the gradient may be smaller than 5 ADU, but during long exposures, it may become e.g. 50 ADU. The broad overscan regions allows for excellent tracking and correction of this structure, as demonstrated in figure 17.

11 Dark current and saturation residuals

The CCD is on the "non-AIMO type, meaning that it does not invert all phases during integration to minimise dark current. This requires the detector temperature to be cooled to $-120°C$ in order to suppress the dark current sufficiently for RON-limited noise in long exposures.

On four occasions, the dark current was measured, using up to six hours for each. The results are somewhat confusing, as dark currents from 4.4 to 19e^-/pixel/hour were found. Each measurement had high internal consistency, giving an uncertainty of 1e^-/pix/h at most. This clearly makes the measurements incompatible. Most images had an illumination pattern that suggested that they were influenced from stray light to some degree. Also, measurements on another CCD from the same batch indicated a dark current of only 0.4e^-/pixel/hour. In all, a reliable determination of the dark current has not been made.

A fraction of the exces dark current observed above may have been residual charge, the remnant of a previous over-exposure. Such charge may slowly leak into the imaging pixels several hours after a saturation.

A seperate test was made by imaging a point source onto the CCD, at a level of 3Me^- per pixel, more than ten times the saturation limit, producing severe vertical charge blooming. The dark current in the affected area was monitored afterwards, and no extra signal was found.

While the test above was negative, a significant residual image could be provoked by saturating the entire device at once, e.g. by strong flat field illumination. A dark exposure after saturation is shown in figure 18. The residual charge is unevenly distributed, strongest along the sides.

It was found that the residual charge could be eliminated by inverting all phases in the imaging area for a short while. This is done by the script below. It is recommended that the script is run after every incident of heavy saturation of the device. Be careful not to corrupt the script, as this may influence the performance of the CCD in all following exposures.

```
@VCLK24-09500
@VCLK25-09500
@VCLK26-09500
@VCLK27-09500
@VCLK28-09500
@VCLK29-09500
sleep 1
@VCLK24-08000
@VCLK25+03000
@VCLK26-08000
@VCLK27+03000
@VCLK28-08000
@VCLK29+03000
```

The camera is equipped with a pressure sensor that as a side-effect emit a small amount of light. The sensor has been baffeled internally to suppress this, and it has not been possible to

find any emmission from the sensor in the dark exposures.

12 Camera house and cooling

The camera is equipped with a Cryotiger cooling system, which eliminates the need for liquid Nitrogen refilling. When cooling from room temperature, the slower cooling rate of the Cryotiger will cause some delay before cryo-pumping of the internal charcoal getter becomes effective. For this reason, the adopted practice here has been to pump down to about $10^{-}4$mBar, start the Cryotiger, and then continue pumping for about half an hour. At this point, the cold finger will be at approximately -170°C and the detector around -30°C. When the pump is stopped at this time, the pressure should not rise much during the rest of the cool down. Cool down from room temperature to operating temperature of -120C is two hours.

In our experience, the vacuum performance with the Cryotiger does not become quite as good as with LN_2, and a pressure about $10^{-}5$mBar should be expected during operation. A Helium leak test revealed a slight fault around the CCD vacuum connector. The leak was considered small enough to not cause problems, but if the vacuum turns out to be inadequate, attention should be brought to this part.

Be careful when handling the vacuum valve: The valve can be opened by a very slight twist of the grip, requiring little force.

The cold braid between the cold finger and CCD mount is very thick, and if the temperature control is disabled while cooling is on, the CCD will be cooled to at least -150°. Also due to the thickness of the braid, the detector temperature cannot be locked to a setting warmer than -100°C.

There has been some concern about loss of pressure of the cooling agent. For reference, here is some of the history of the FIES Cryotiger.

Situation	*Pressure*	*Comment*
At delivery	>320psi	Needle towards stop!
After mounting of hoses	310psi	Excluding de-humidifier
After first cooling	295psi	
After second cooling	294psi	
After dismounting of hoses	294psi	

In long dark exposures in the laboratory basement, the hit rate from energetic particles, "cosmics", was found to be 76 ± 2 hits/cm^2/hour. From our statistical material, this appears to be a normal rate, i.e. there is no significant contribution to the hit rate from radioactive materials in the cryostat.

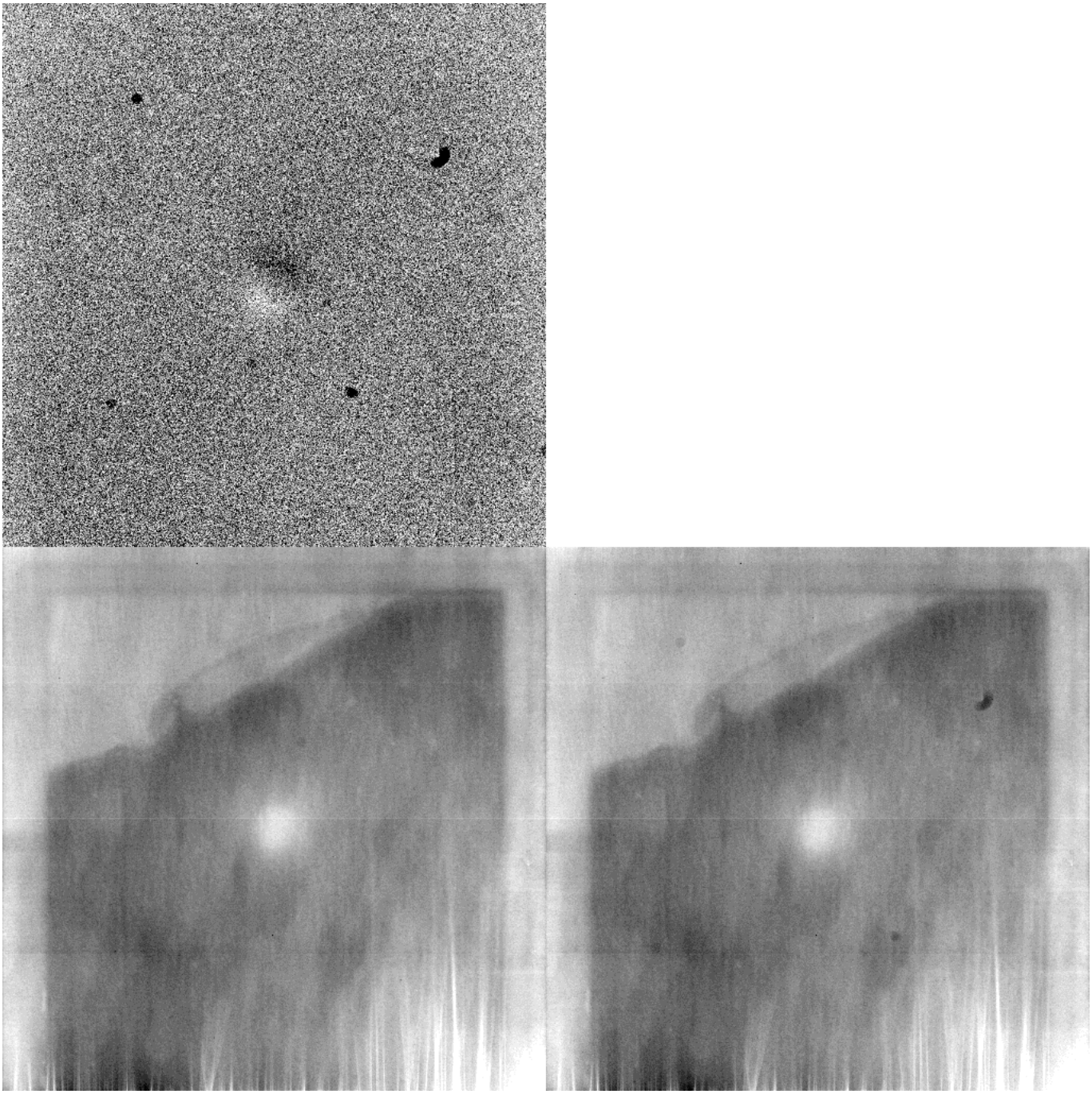

Figure 1: Flat field properties at 1060nm. *Lower left:* The greyscale cuts are set to ±8% of the median level. *Lower right:* Five days later. *Top:* Ratio between the two flat fields, displayed with cuts of ±1%. The local differences is due to new dust specks arriving and a changed distribution of scattered light.

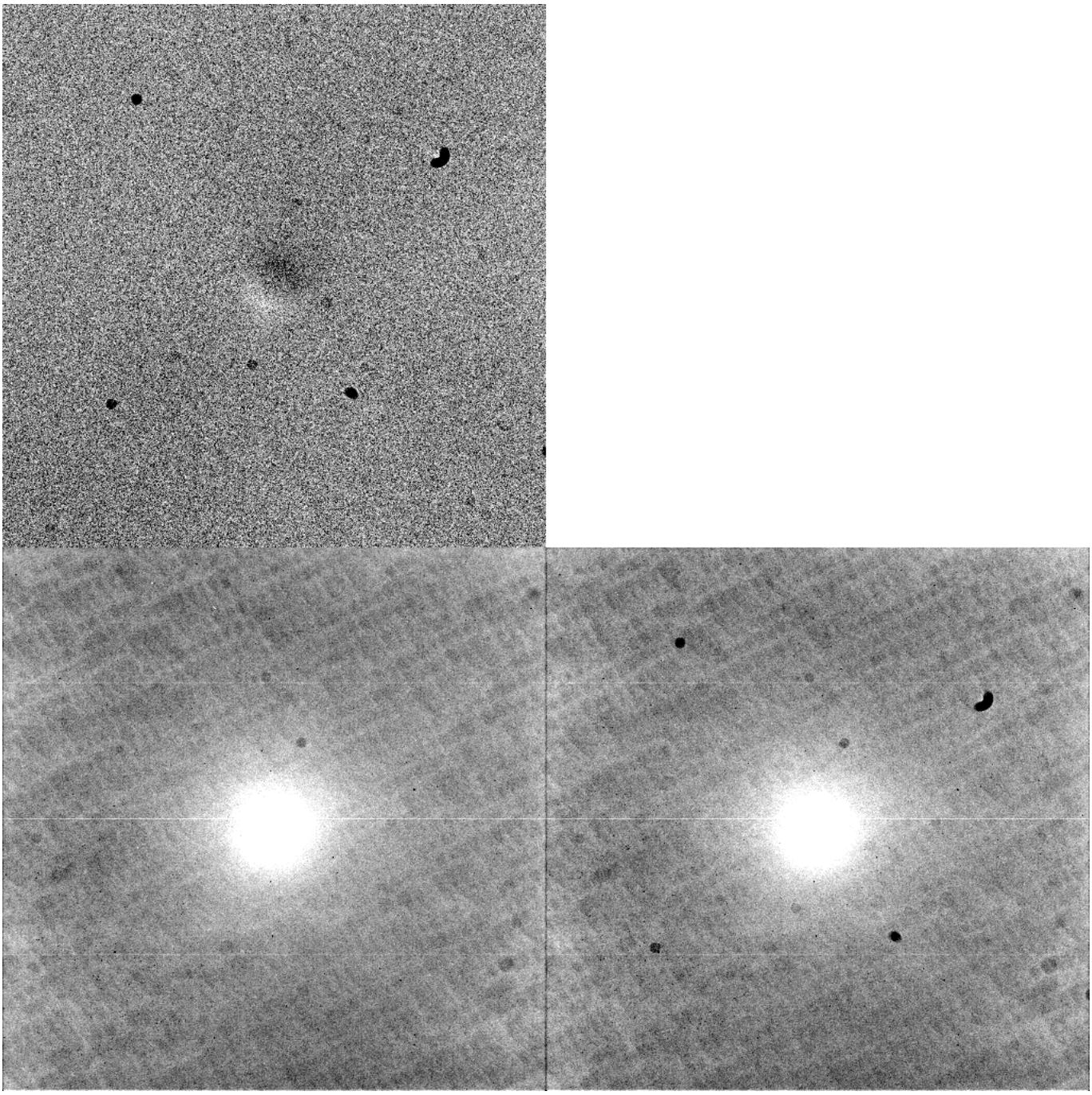

Figure 2: Flat field properties at 550nm. *Lower left:* The greyscale cuts are set to ±2% of the median level. *Lower right:* 5 days later. *Top:* Ratio between the two flat fields, displayed with cuts of ±1%.

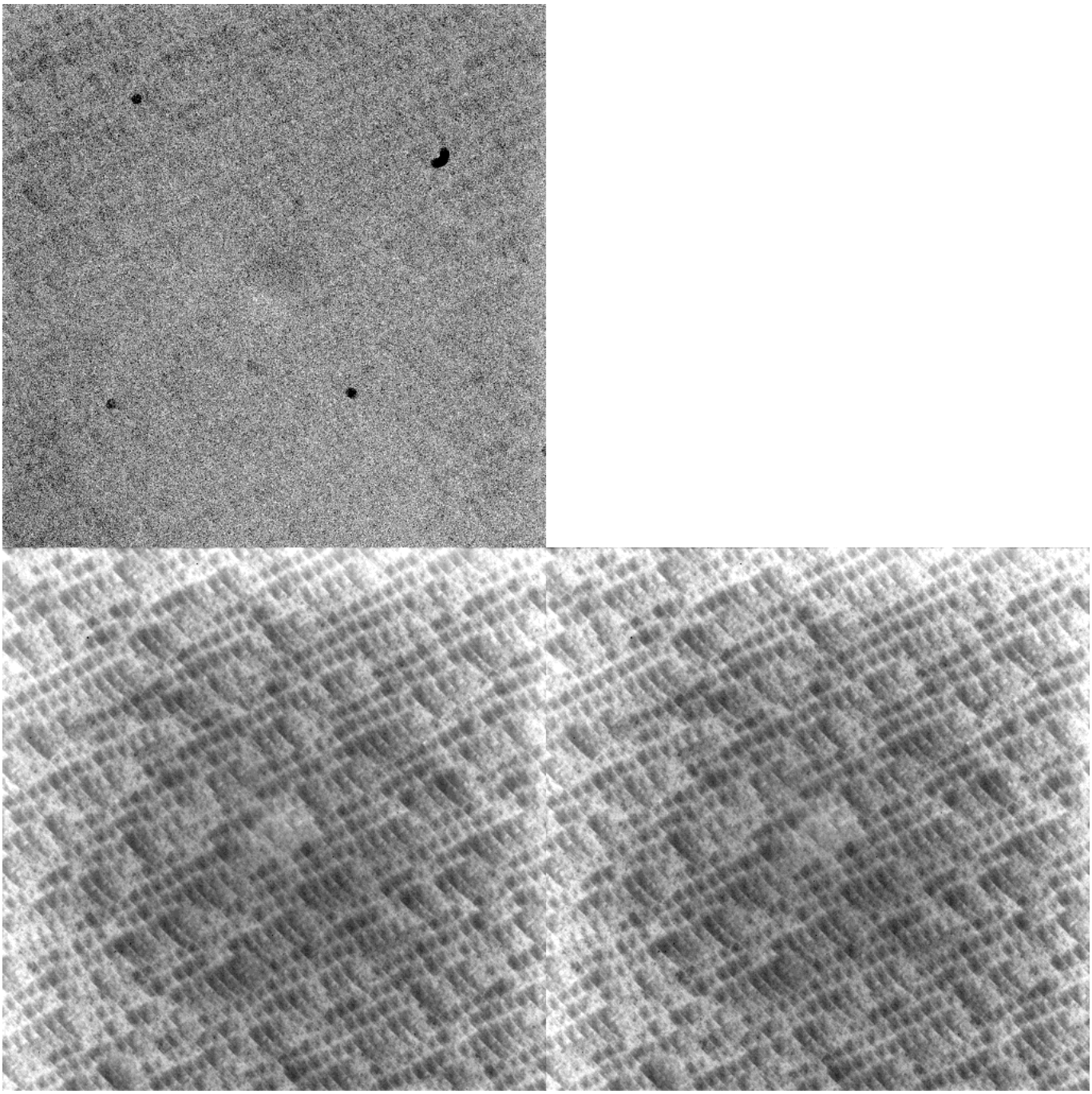

Figure 3: Flat field properties at 334nm. *Lower left:* The greyscale cuts are set to ±15% of the median level. *Lower right:* 5 days later. *Upper left:* Ratio between the two flat fields, displayed with cuts of ±2%.

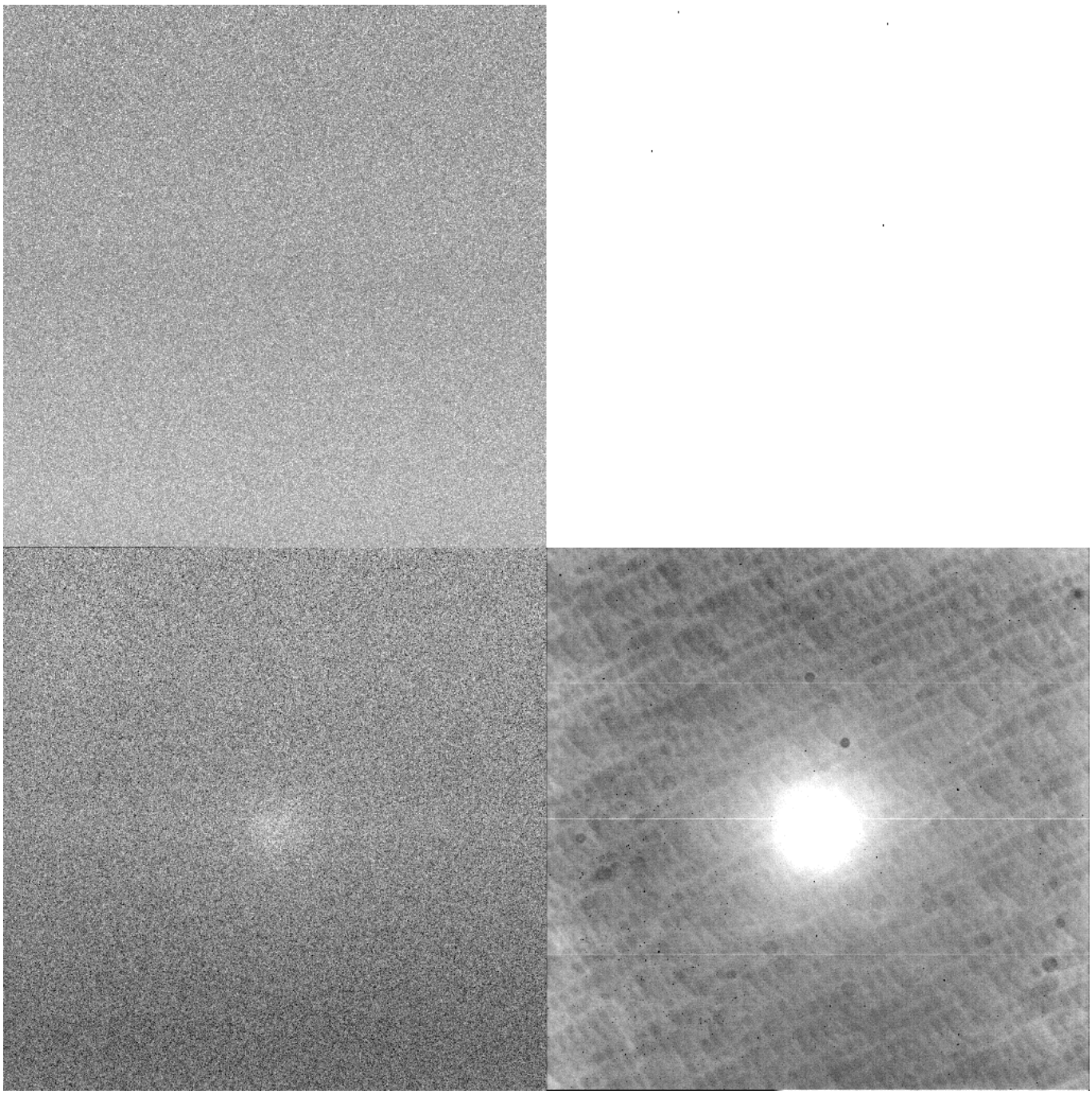

Figure 4: Low illumination level flat field properties, as a mean of identifying charge traps. *Lower left:* Flat field at an illumination level of $20e^-$/pixel. Grey scale cuts are ± 20% of median level. Signal is mostly seen as shot noise. Traps would have been visible as dark vertical lines, but none are found. *Lower right:* Flat field at an illumination level of $24.500e^-$/pixel. Grey scale cuts are ± 2% of median level. *Upper left:* Ratio of the two flat fields. Grey scale cuts are ± 30% of median level. *Upper right:* Deviating points in the ratio image, affected by traps.

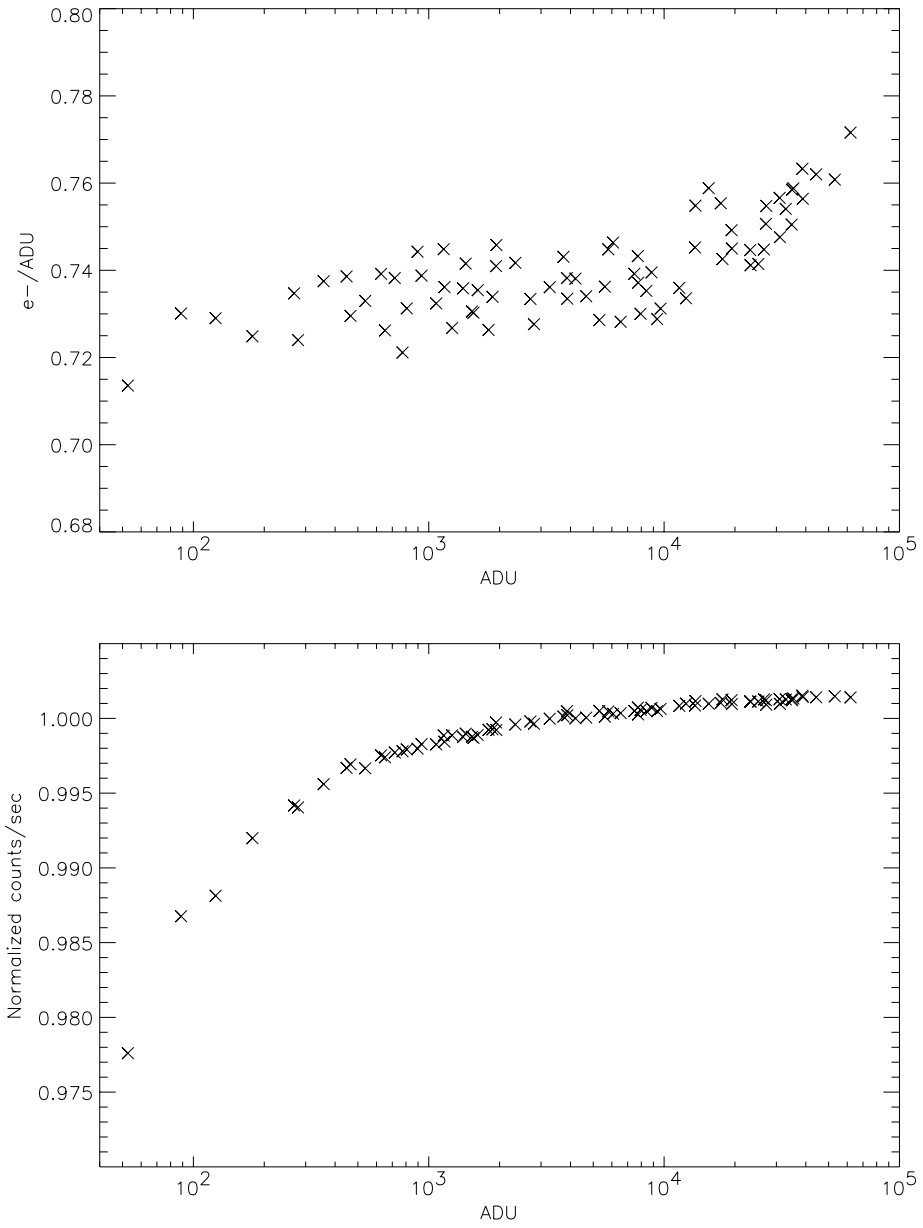

Figure 5: Linearity data for amplifier A in high gain mode. *Top:* Gain versus exposure level measured from noise statistics. *Bottom:* A plot of ADU per second versus total exposure time, corrected for shutter delay.

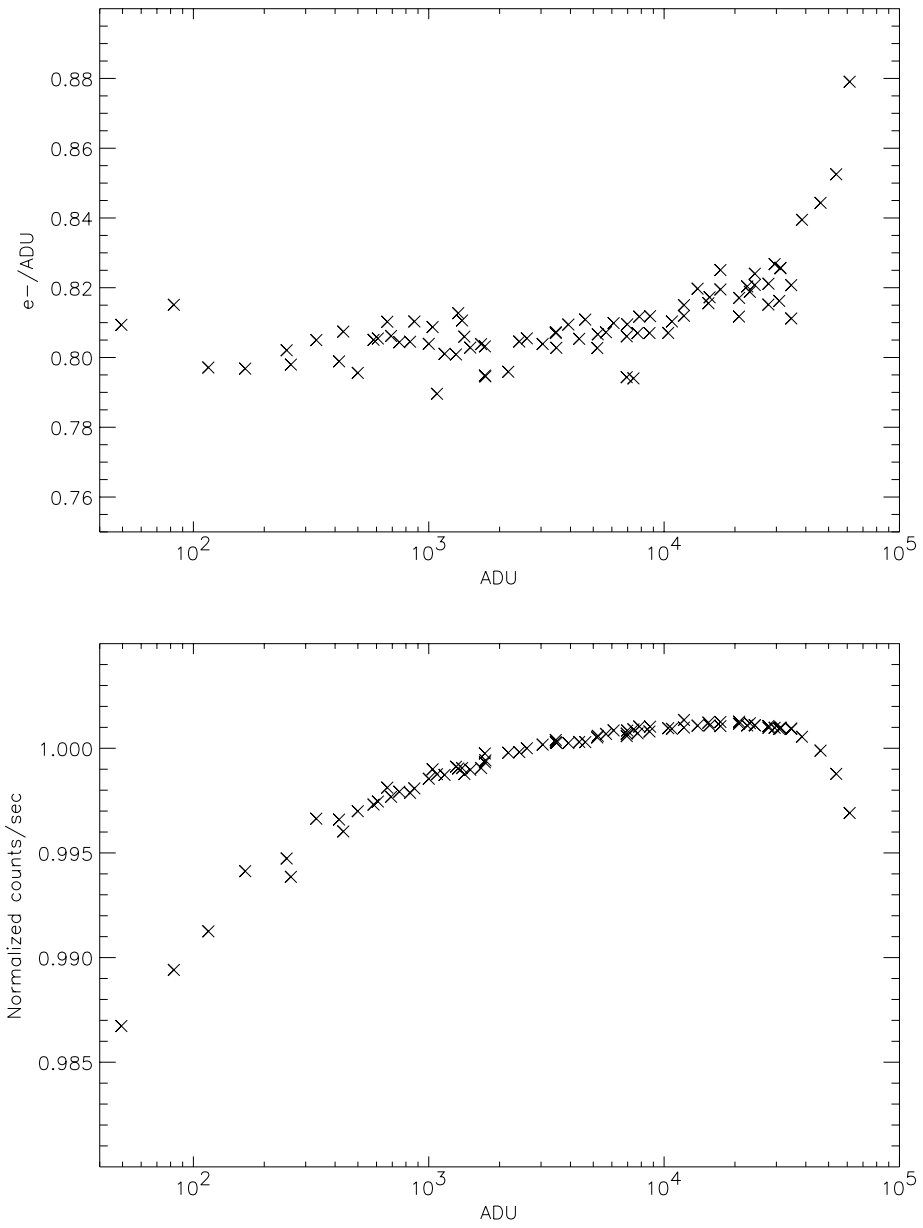

Figure 6: *Top:* Gain versus exposure level measured from noise statistics for amplifier B in high-gain mode. *Bottom:* A plot of ADU per second versus total exposure time, corrected for shutter delay. Data is again for amplifier B in high-gain mode.

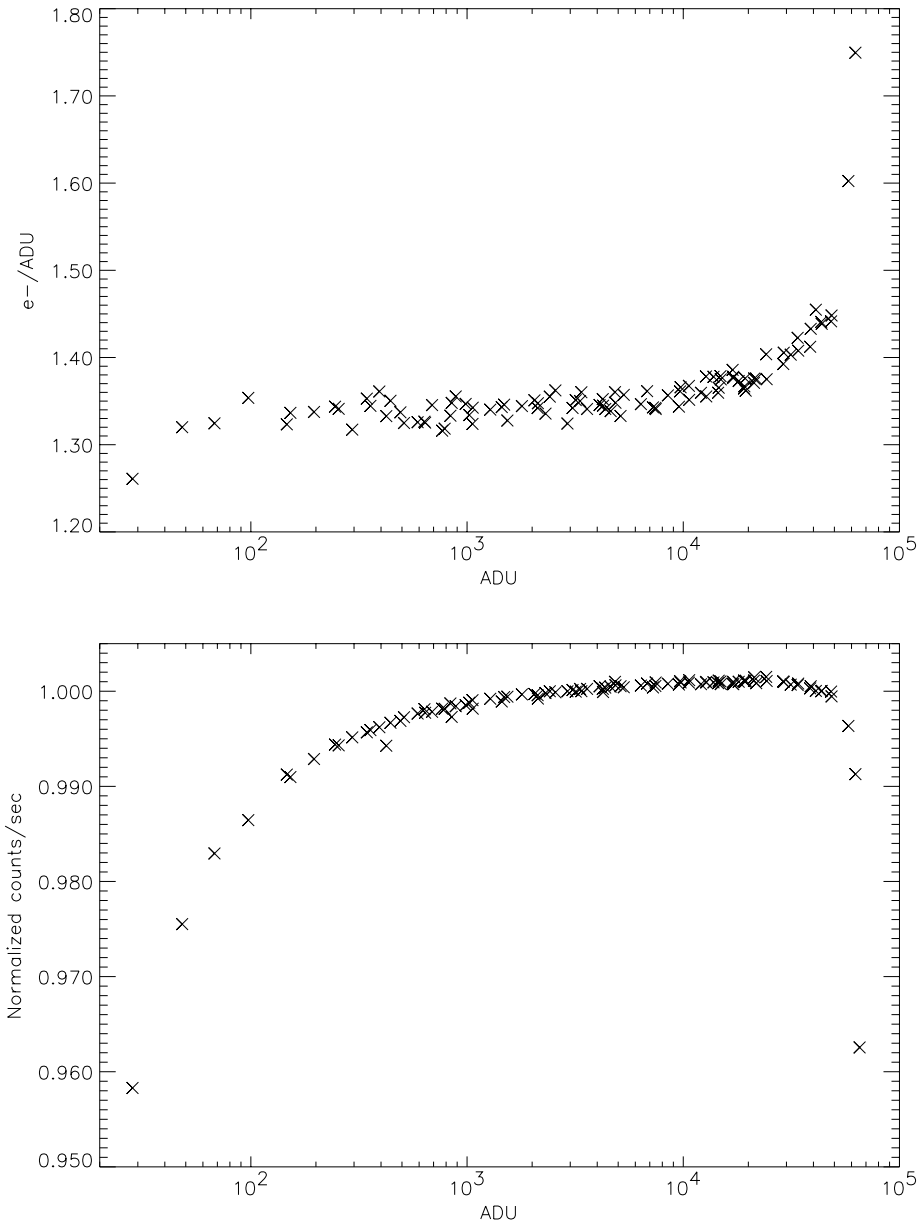

Figure 7: *Top:* Gain versus exposure level measured from noise statistics for amplifier A in low-gain mode. *Bottom:* A plot of ADU per second versus total exposure time, corrected for shutter delay. Data is again for amplifier A in low-gain mode.

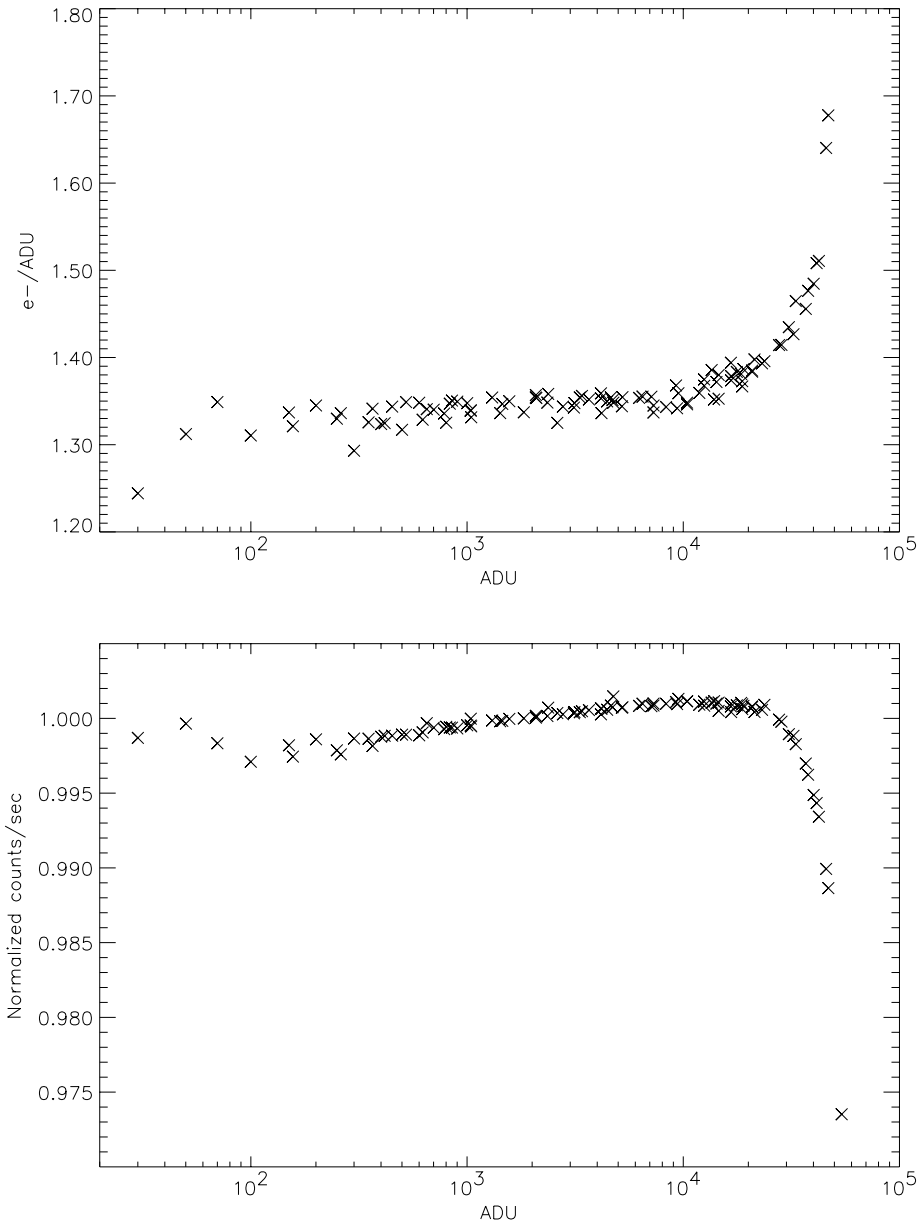

Figure 8: *Top:* Gain versus exposure level measured from noise statistics for amplifier B in low-gain mode. *Bottom:* A plot of ADU per second versus total exposure time, corrected for shutter delay. Data is again for amplifier B in low-gain mode.

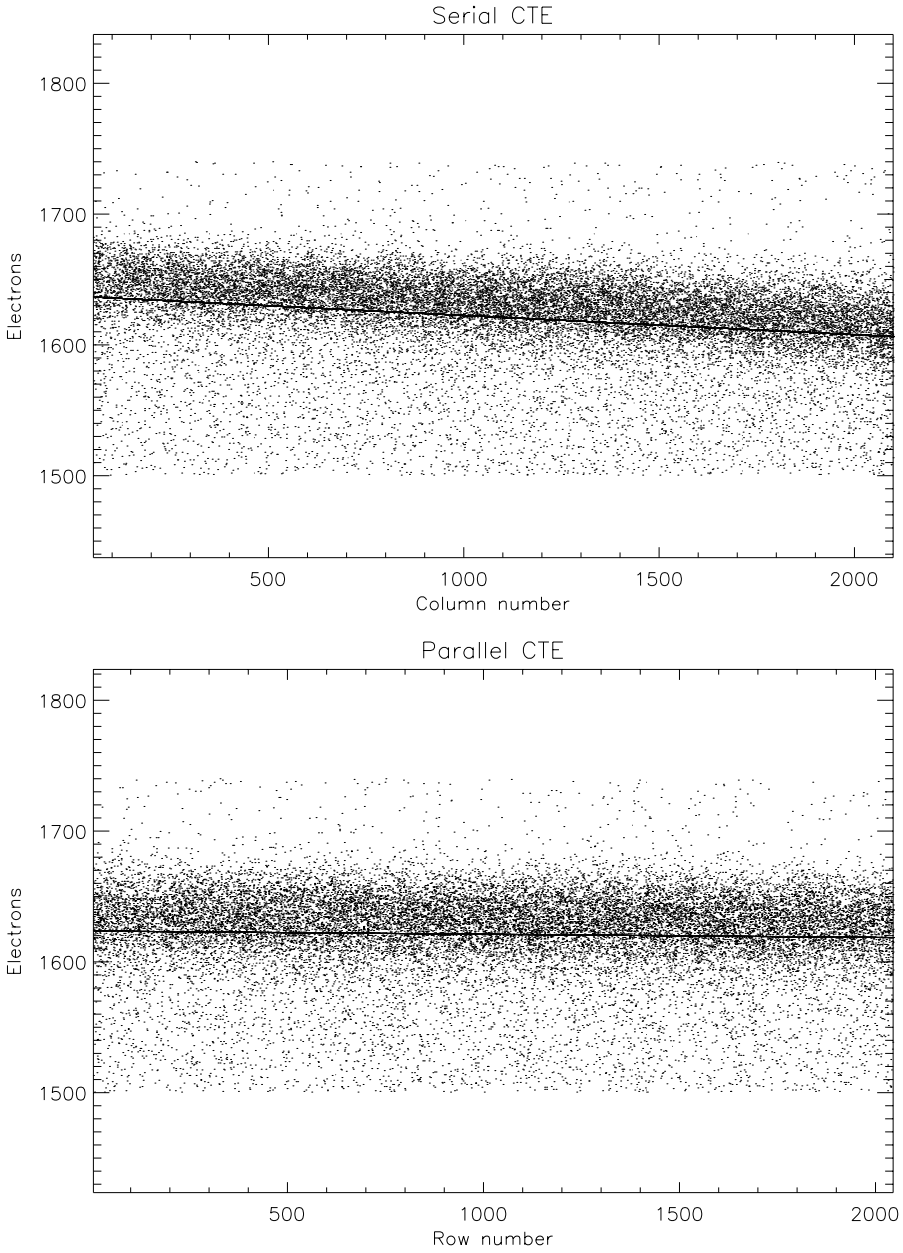

Figure 9: Plot of ^{55}Fe K-α peak counts versus row and column position, used for measuring CTE. The gradient along the rows shows a slight loss during serial transfers, while parallel shifts are near perfect.

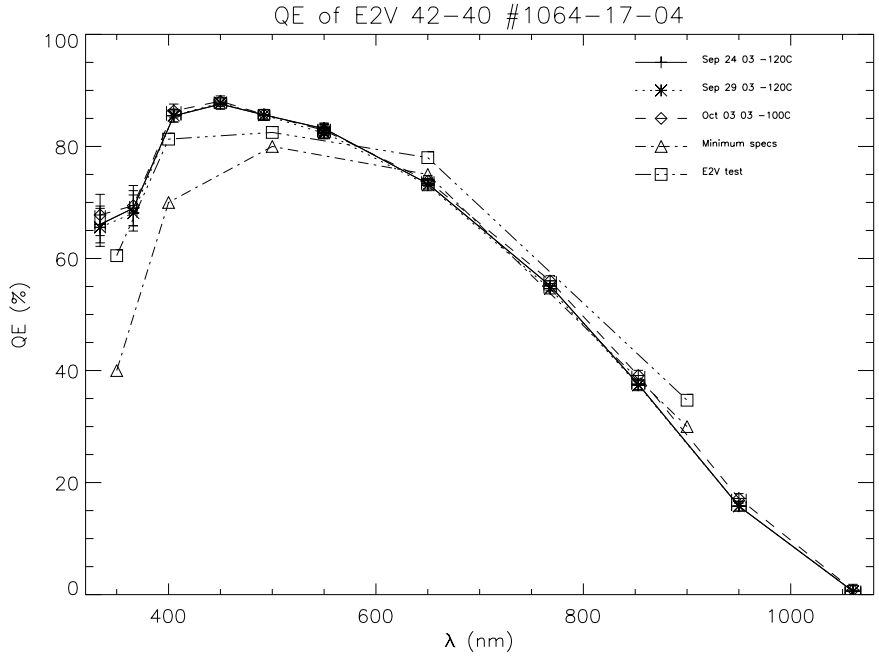

Figure 10: Quantum efficiency versus wavelength for the CCD42-40 at $-120°C$, measured twice at -120°C and, slightly above, at -100°C. These are drawn with horisontal bars marking filter FWHM and vertical bars showing the Pixel Response Non-Uniformity. Also shown are E2V minimum specifications (triangles) and test data (squares) at $-30°C$.

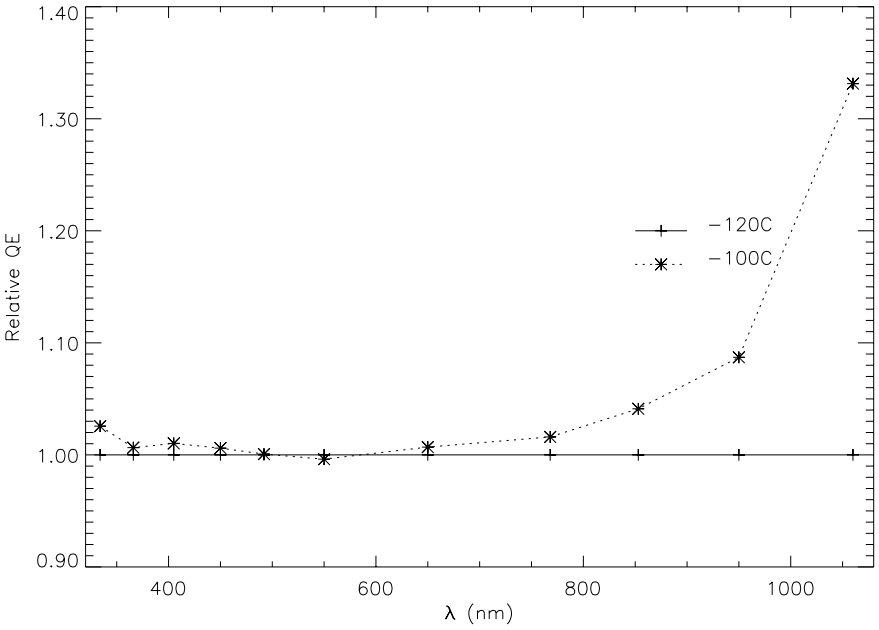

Figure 11: Quantum efficiency at -100°C plotted relative to the QE at -120°C. The improvement in QE from going to higher temparatures is quite large in the near-infrared.

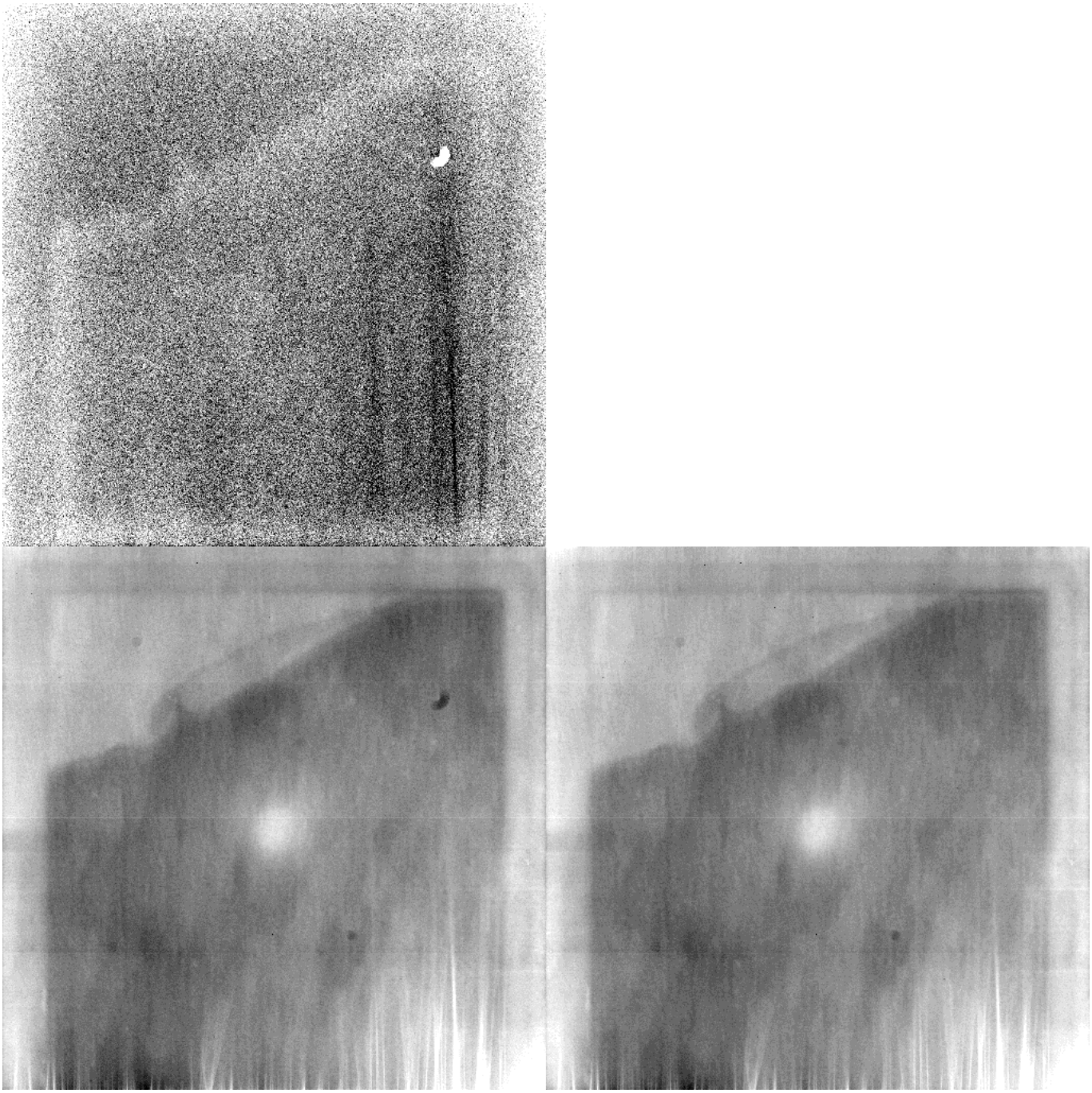

Figure 12: Flat field dependency on temperature at 1060nm. *Lower left:* CCD at -120°C. The greyscale cuts are set to ±8% of the median level. *Lower right:* CCD at -100°C. *Top:* Ratio between the two flat fields, displayed with cuts of ±1%. In the lighter areas, the QE has increased at -100°C relatively to -120°C. Also, a dust speck has moved and the refections off the bonding wires have changed.

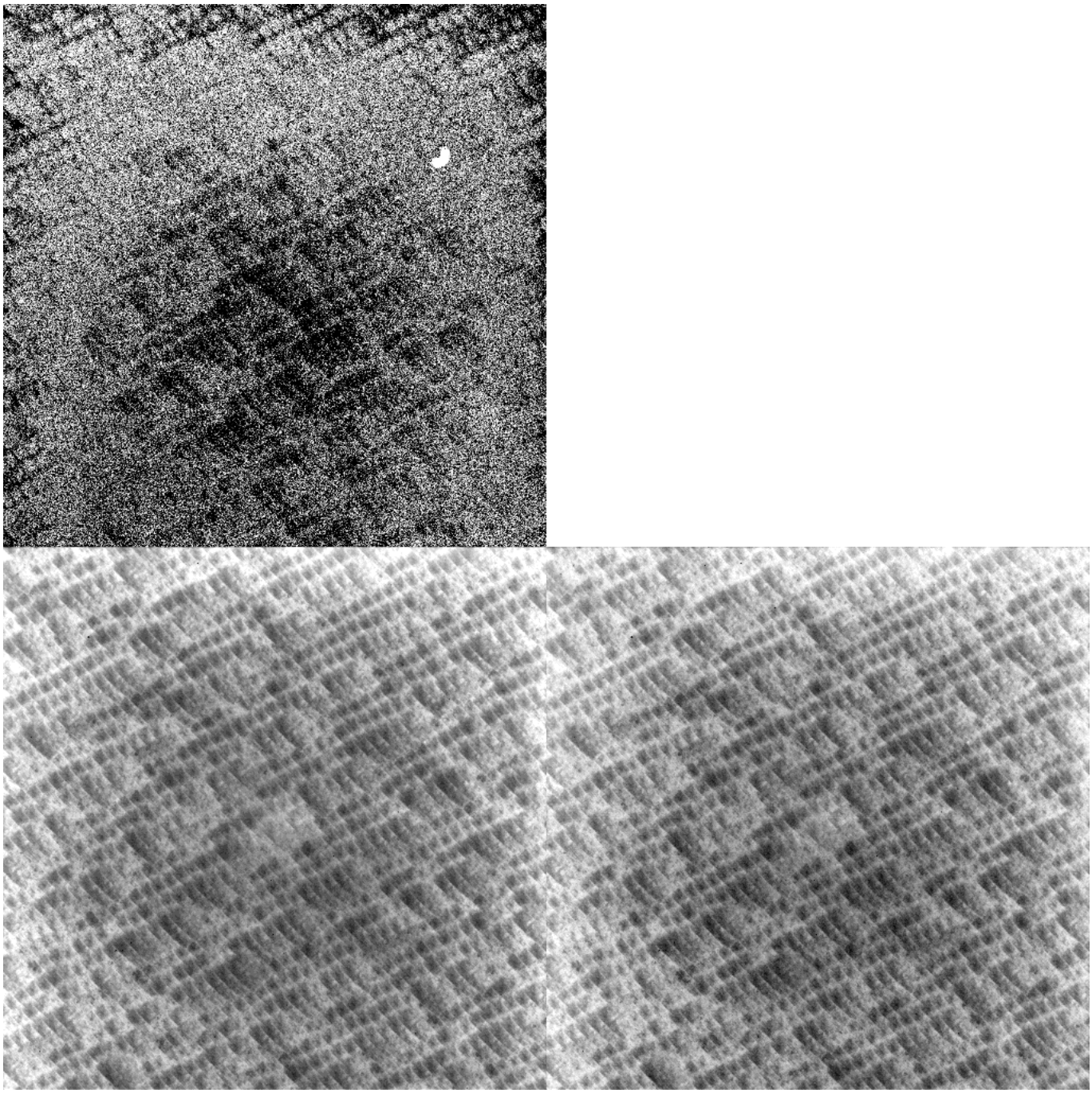

Figure 13: Flat field dependency on temperature at 334nm. *Lower left:* CCD at -120°C. The greyscale cuts are set to ±15% of the median level. *Lower right:* CCD at -100°C. *Upper left:* Ratio between the two flat fields, displayed with cuts of ±1%. In the lighter areas, the QE has increased at -100°C relatively to -120°C.

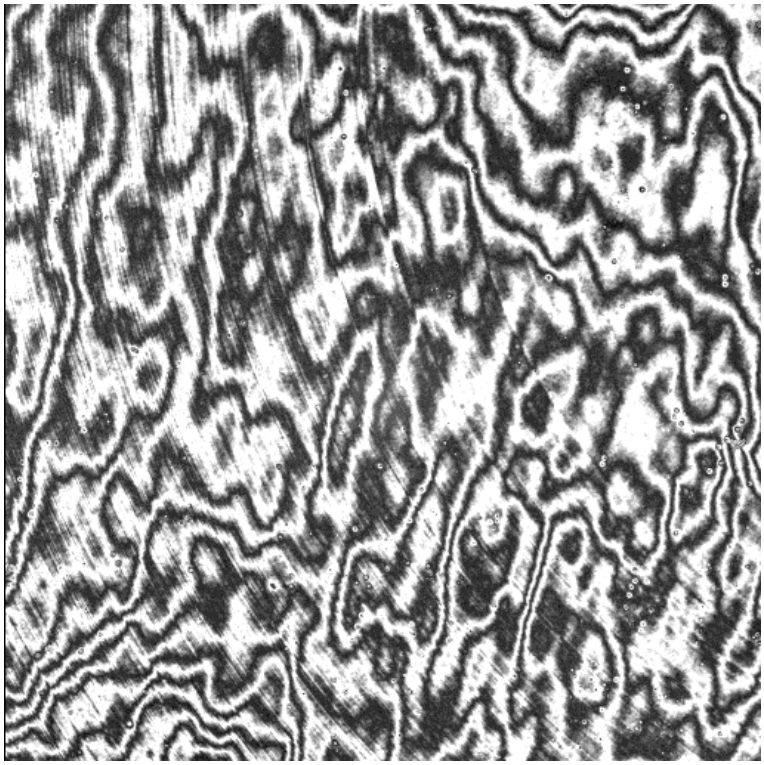

Figure 14: Fringing from 830nm laser illumination. The greyscale cuts are set to ±30% of the median level.

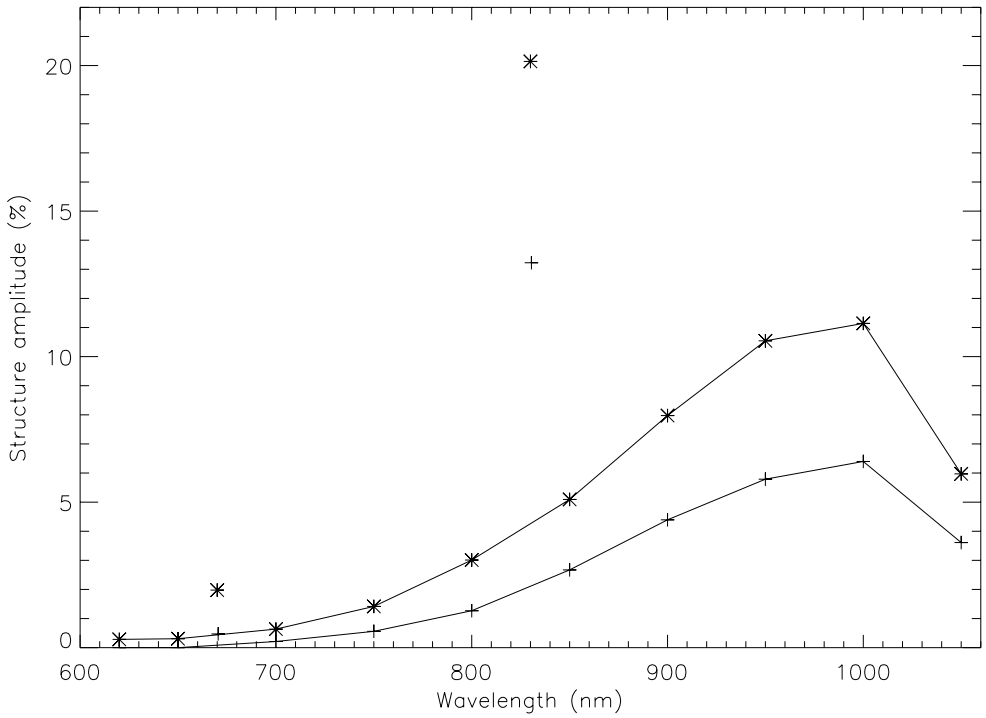

Figure 15: Fringe amplitude dependence on wavelength for two CCD42-40's. The curves are for monochromator data, and the isolated points laser data.

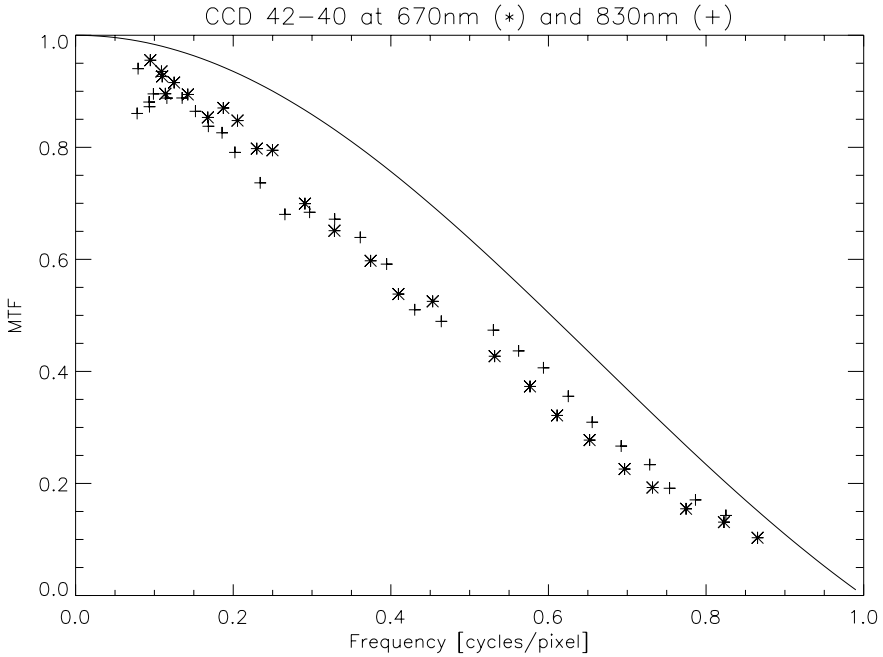

Figure 16: Plot of MTF at two wavelengths for the CCD42-40. Stars represent 670nm illumination and plusses 830nm.

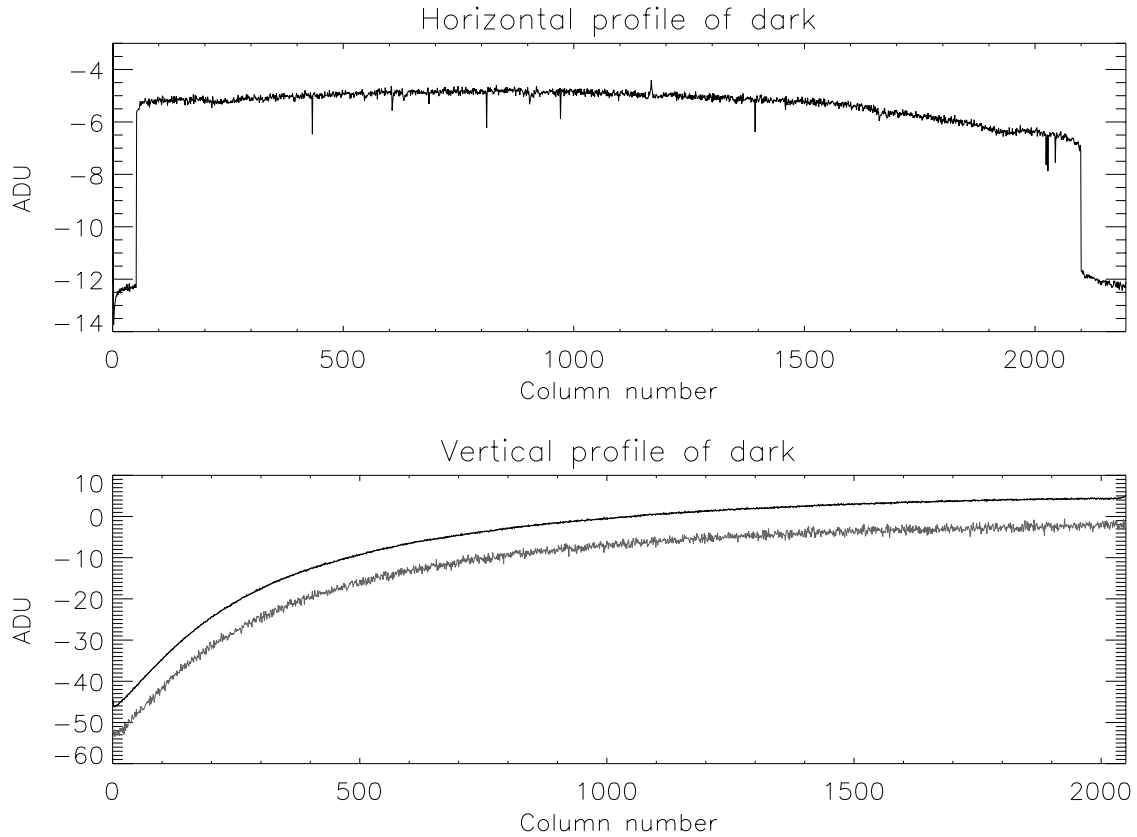

Figure 17: Horisontal and vertical profiles of the combination of several 1800sec dark exposures. In the horisontal profile, 50 pixels on each side of the imaging area trace the bias level, and on the right side further 50 pixels of artificial overscan are created by continued read-out beyond the length of the serial register. In the vertical profile, the narrow black graph is the dark level and the noisier grey graph is the overscan level.

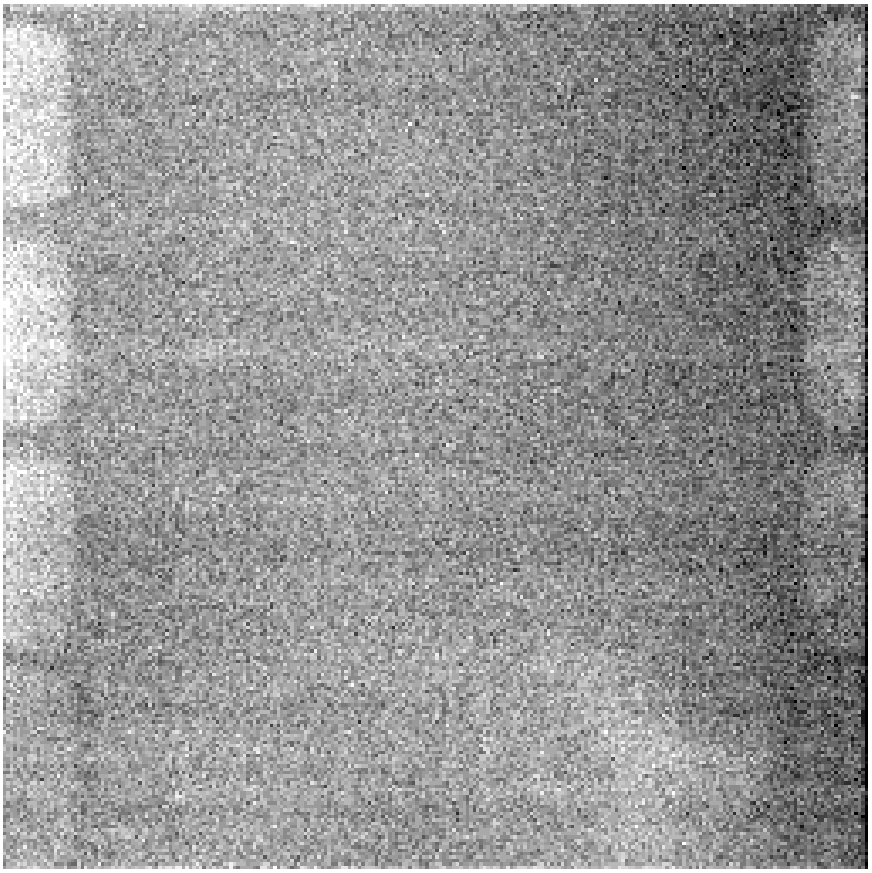

Figure 18: Dark current and residual image distribution for an 1 hour measurement using 4 by 4 pixel binnig. The average level is $8.8e^-$/pixel/hour, but some variation can be seen. At both sides, bands with increased flux appear, along with a triangular structure in the lower right corner. There are no hot pixels or columns to be found.